ChemComm



COMMUNICATION

View Article Online
View Journal | View Issue



Cite this: *Chem. Commun.*, 2017, 53, 4930

Received 6th February 2017, Accepted 10th March 2017

DOI: 10.1039/c7cc00964j

rsc.li/chemcomm

Thermally driven bubble evolution at a heater wire in water characterized by high-speed transmission electron microscopy†

J. R. Vance and S. J. Dillon*

This work investigates the early stage evolution of thermally nucleated microbubbles in water using *in situ* high-speed, 400 fps, transmission electron microscopy. A Pt wire Joule heater induced bubble nucleation and growth from air-saturated water at different levels of power. For all powers below Pt breakdown, the dissolved gas initiates bubble nucleation at the concave surface defects adjacent to the area of highest temperature. A combination of interfacial forces and stress relaxation drive rapid migration of the bubbles away from the nucleation site. Thermocapillary forces ultimately dominate and drive their return to the region of highest temperature. The dynamic response highlights the importance of this length and time domain, which has until now received limited direct study.

Bubbles govern the evolution of diverse physical and chemical processes near liquid-solid interfaces, often acting as important mediators of chemical and energy fluxes. While large bubbles have been investigated extensively for over a century, the behavior of bubbles less than several microns in diameter has yet to be systematically explored. With nanofluidic systems receiving greater experimental and practical applications, it is important to understand bubble dynamics at small length and time scales. At large surface-area-to-volume ratios, interfacial thermodynamics dominate leading to dynamics and stabilizing mechanisms not found in larger bubbles.² The utility of microbubble generation and control has been noted in active microfluidic and microelectromechanical systems³ with bubbles serving as elements including valves, actuators, and pumps. 4 Predicting and controlling microbubble response is key to the design and optimization of such systems. For example, spatially dependent thermocapillary forces can be produced using arrays of resistive heaters⁵ or laser illumination,⁶ and allow for a precise control of bubble motion. These can be applied to such tasks as particle manipulation/trapping⁶ as well as flow control. Similar mechanisms should prove useful in

Department of Materials Science and Engineering, University of Illinois at Urbana-Champaign, 1304 W. Green St., Urbana, IL 61801, USA. E-mail: sdillon@illinois.edu

† Electronic supplementary information (ESI) available: Thermodynamic modeling, Fig. S1–S6 and Video S1. See DOI: 10.1039/c7cc00964j

fluidic devices with sub-micron critical dimensions. In addition, the performance of heat exchangers can be improved, with metastable nanobubbles at nanostructured interfaces shown to enhance heat flux during water boiling.^{8,9}

Microbubble evolution during water boiling is a key example, of interest in practical heat-transfer systems and as a prototype for the study of phase transformation and bubble phenomena. The heterogeneous evolution of water vapor bubbles is driven by superheating at liquid-solid interfaces, with interfacial energies, gas cavities, and heater geometry significantly affecting the energy landscape for bubble nucleation. 10,11 After nucleation, energy gradients and hydrodynamic effects control bubble migration and growth. At small radii, surface tension effects and resulting interfacial forces, including contact angle and thermocapillary flow at the water-vapor interface, dominate over the buoyant force that drives microbubble detachment. These result in phenomena including critical heat flux, coalescence and oscillatory motion. 10 Temperature dependent water-vapor surface tension creates liquid flows at interfaces (the thermocapillary effect), driving microbubbles up thermal gradients.³ Thermally driven microbubble evolution at resistive heaters has been a popular subject for experiment. Microbubble sweeping, detachment, and return at microwire heaters have been observed, with velocities greater than 50 mm s⁻¹ and oscillatory behavior at the millisecond timescale.12 The importance of temperature, heating rates, and heater dimensions to microbubble nucleation has been shown.13 The behavior of microbubbles subject to thermal gradients in confined geometries has also been studied, including in microchannels14 and Hele-Shaw15 cells most analogous to nanofluidic devices and liquid cells used in transmission electron microscopy (TEM).

As the spatial resolution of conventional photomicroscopic techniques is limited by the wavelength of light, most work investigating microbubble phenomena has focused on diameters larger than several microns, The gap in understanding at the small scale has gained increasing experimental attention, prompted by discoveries of nanobubble stability ill-predicted by classical theory.² These works typically employed indirect

Communication

methods, including scattering techniques 16,17 and nanoelectrodeblocking, 18 or used atomic force (AFM)19 or liquid cell (scanning) transmission electron microscopy ((S)TEM)²⁰⁻²² to image relatively long-lived bubbles. Other depth sensitive optical techniques, including total-internal-reflection microscopy²³ and surface plasmon resonance²⁴ also allow for the selective probing of nanobubbles at the solid-liquid interface. Regan's group observed bubble evolution at a heating wire in liquid cell STEM, but the nucleation site and other millisecond-scale dynamics were not observable due to limited temporal resolution.21 AFM and (S)TEM typically have acquisition times on the order of several seconds and 100 ms or more, respectively, preventing useful imaging of fast dynamics. In TEM experiments, electron beam induced heating and radiolysis must be taken into account, 20,25 but these can be limited with low beam intensity and proper selection of sample chemistry. Recently, commercial high frame-rate direct electron detectors have become available, 26 allowing for routine in situ imaging with millisecond temporal resolution. Here we present the application of high-speed TEM for characterization of thermally induced bubble evolution in water with the aim of filling a critical knowledge gap with respect to the evolution of such bubbles in the micron scale length and millisecond time regimes.

A commercial three-electrode liquid flow cell holder and associated chips containing 50 nm amorphous SiN_r windows (Hummingbird Scientific) were employed. A Pt heater wire (length $\approx 20 \, \mu \text{m}$, width $\approx 500 \, \text{nm}$, resistance $\approx 850 \, \Omega$) was deposited using a scanning electron microscope (FEI) from trimethyl(methylcyclopentadienyl) platinum precursor gas onto the bottom window, using pre-patterned Pt electrodes as electrical traces. The wire was annealed for 30 min at 450 $^{\circ}\mathrm{C}$ in air to reduce carbon byproducts inherent to the e-beam deposition process and improve conductivity. Prior reports indicate that such a heat treatment should reduce the carbon concentration to $\approx 10\%$. Scanning electron micrographs of the bottom window with features labeled before and after heater wire deposition are reproduced in Fig. S1 (ESI†). Before assembly, the windows were given a hydrophilic surface functionalization by oxygen plasma. A droplet of airsaturated ASTM Type 2 deionized water (VWR) was pipetted onto a second window with a 250 nm spacer, and the cell was assembled, with an estimated liquid layer thickness of $\sim 500-1000$ nm. The liquid cell was imaged in a Hitachi H-9500 TEM at 300 kV using a K-2 IS direct electron detector (Gatan) at 400 frames per s and $1000 \times$ magnification. The smallest spot size was employed (beam current density $\sim 40 \text{ A m}^{-2}$) to minimize radiolysis and beam heating. No beam-induced bubbles were observed during the experiments, these being typically observed only for beam current densities $> \sim 300 \text{ A m}^{-2}$. A potentiostat (Bio-logic) was used to power the heater wire for 10 s at 0.01, 0.05 0.10, 0.50, and 1.00 V (<1.20 V to prevent electrolytic effects), with the interior of the liquid cell at atmospheric pressure and room temperature. A schematic of the experimental setup and beam path is given in Fig. S2 (ESI†). Between experiments, a syringe pump was used to flow fresh deionized water through the cell to displace bubbles from the windows, allowing for repetition without cell reassembly.

At 0.10 V and above, bubbles regularly nucleated in the vicinity of concave defects in the middle platinum trace (see Fig. S3a, ESI†),

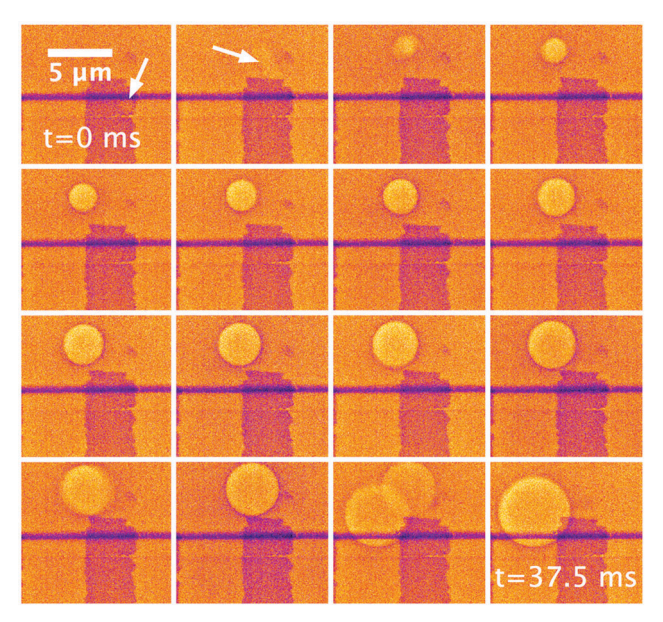


Fig. 1 Time-lapse in situ TEM images showing the initial bubble growth and dynamics (2.5 ms between frames). The arrows in the first two images indicate the position of the bubble, which initially moves rapidly and is thus imaged with motion blur.

which formed fortuitously during handling, near the center of the heater wire and adjacent to the area of maximum temperature (see Fig. S4, ESI†). Below 0.10 V, no bubbles nucleated. Fig. 1 shows the early evolution of a bubble nucleated under an applied voltage of 1.00 V. Fig. 2A-E reproduces schematically 50 ms of time evolution of the first nucleated bubble in five experiments performed at different voltages, with Fig. 2F plotting bubble diameters vs. time. The bubble position and diameter were determined by selecting the bubble-liquid interface in image sequences with the ThreePoint-CircularROI plugin in ImageJ64. Reproducible behavior is observed for experiments performed using the same heater power. As is characteristic (see Fig. 1, 2A-E and Video S1, ESI†), a bubble nucleates at a defect near the heater wire and rapidly migrates across it and the central platinum trace to the bare silicon nitride window, while growing rapidly. Importantly, in experiments employing a heater window without similar defects present, nucleation was not observed until power levels capable of destroying the heater wire were employed (see Fig. S3b, ESI†). This suggests that defects of radius near the order of metastable nuclei are critical to nucleation. Evidence for this is found in a similar work done using STEM; White et al. hypothesized that no metastable bubble evolution occurred until the collapse of unstable evolved nanobubbles produced a micron scale surface defect.²¹ After initial nucleation, the bubble rapidly bridges the two silicon nitride windows, forming a roughly symmetric cylindrical segment, with a constant mean curvature and water contact angle of less than 90° (the windows are hydrophilic). The growth of the bubble is driven by thermally induced degasification and water evaporation. Migration to the center of the SiNx window is likely driven by the confluence of capillary forces (i.e. wetting on SiNx versus Pt), momentum transfer, and relaxation due to outward bowing of the SiN_r windows that relieves pressure. The bubble then abruptly reverses course as the

ChemComm Communication

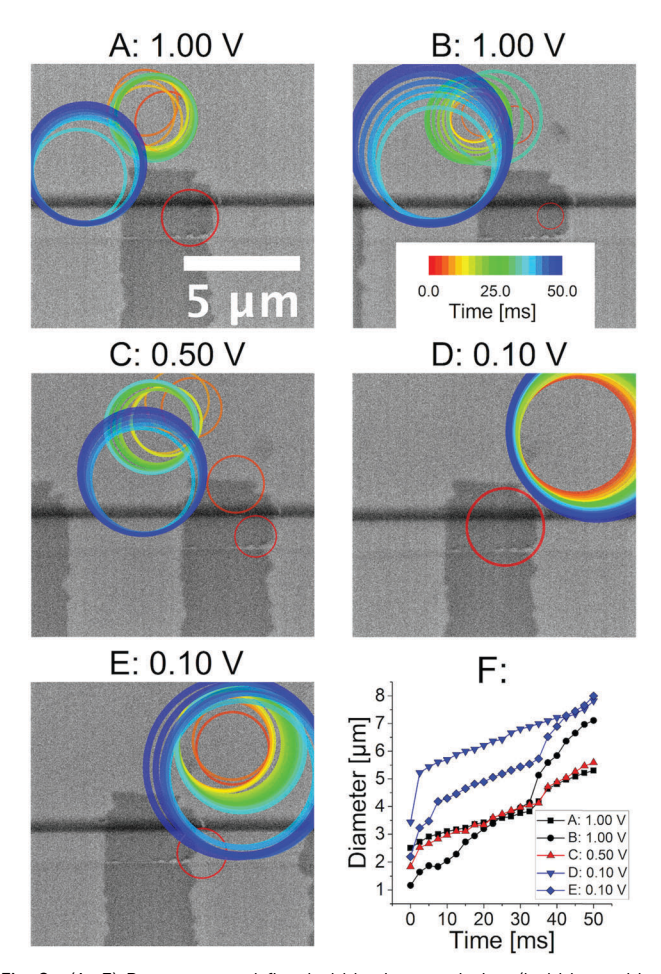


Fig. 2 (A-E) Reconstructed first bubble time evolution (bubble position and size vs. time) in experiments A-E, (F) first bubble diameter vs. time after first nucleation in experiments A-E.

surrounding liquid continues to heat and thermocapillary forces become dominant. The bubble then migrates up the temperature gradient and reattaches to the heater wire in the vicinity of the maximum temperature. From this point, it continues to grow until it covers the wire.

To determine whether the evolved bubbles are due to water boiling or the liberation of dissolved gas, we must consider the supersaturation of dissolved gas and the available superheat for water vaporization. Prior to irradiation and heating, dissolved gas in air-saturated water consists almost entirely of O2 and N2 (0.5 and 0.3 mM, respectively).28 The electron beam drives a system of reactions, with O2 and H2 molecules as significant products. As most work with electron radiolysis in water has considered dose rates several orders of magnitude less than those found in liquid cell TEM, complex kinetic models must be employed to extrapolate dissolved gas concentrations. At the employed beam current density of $\sim 40 \text{ A m}^{-2}$, electron accelerating voltage of 300 kV, and room temperature, Schneider et al. predicted total dissolved gas concentration of approximately 1 mM, and a steady-state relaxation time of ~ 10 ms.²⁵ As the water adjacent to the heater wire increases in temperature, the solubilities of these gases decrease, making gas evolution more favorable. At the lowest applied voltage with visible nucleation, 0.10 V, finite element modeling (COMSOL), shown in Fig. S4 (ESI†), predicts a maximum temperature \approx 98 °C, with gas nucleation occurring in the adjacent lower temperature regions. Under these conditions it is difficult to state unequivocally whether the gas bubble is water vapor or dissolved gas. Examining the steady state concentrations of H₂, O2, and N2 (see Fig. S5, ESI†) at temperatures below the boiling point of water, we find vapor pressures much larger than that of water. The volume ratio of dissolved gas to water is \sim 2% at room temperature and steady state, which is not enough to fully supply the bubbles observed here after significant growth. However, with rapid diffusion $(D > \sim 10^{-5} \text{ cm}^2 \text{ s}^{-1} \text{ in the bulk at room temperature})^{25}$ and continuous radiolytic production of gas at greater than atmospheric vapor pressures may be sufficient to support bubble growth without boiling. Dissolved gas is commonly observed to nucleate and grow from water prior to the onset of boiling, and the presence of an electron beam may facilitate this process close to the boiling point.

Evolution during the first 50 ms of bubbles life shows consistent trends, with diameter growing with the square root of time at constant position, and growth rates (see Fig. 2) increasing significantly when the bubble reattaches to the heater wire. The parabolic kinetics suggest that bulk diffusive thermal and gas transport to the bubble interface are limiting. The rapid bubble growth upon attachment of the bubble to the Pt wire should result from H₂O boiling around the liquid-gas-heater intersection. Because nucleation is much faster than our frame rate (2.5 ms) and the bubble migrates rapidly thereafter, its contrast in the first frame is convoluted (see Video S1, ESI[†]). This makes it difficult to prove directly that nucleation is heterogeneous, but the regular proximity of the first visible location of the bubbles to the defects in the middle Pt trace strongly supports this view. Somewhat counter-intuitively, it appears that lower heating power produces higher growth rates and initial nucleus size (see Fig. 2F). This can be explained if we assume that metastable nucleation requires a critical temperature; as it takes longer for the wire to reach this temperature, the thermal gradient in the surrounding liquid will be smaller and the driving forces for gas evolution and water evaporation larger.

We hypothesize that the observed abrupt reversals of the bubble at the center of the window is the result of the thermocapillary force on the bubble overcoming the hysteresis of the contact lines and the relaxation force due to window bowing. The surface tension γ of the water liquid-vapor interface decreases roughly linearly with temperature until it vanishes at the critical point $(-d\gamma/dT = \sim 0.2 \text{ mN m}^{-1} \text{ K}^{-1})$. In a temperature gradient, the liquid at the bubble interface will flow from hot to cold, and the bubble will move up the gradient in temperature. Assuming a linear temperature gradient dT/dx, bubble radius R and thickness t, the approximate thermocapillary force F can be given as:

$$F = 2\pi Rt \times \frac{\mathrm{d}\gamma}{\mathrm{d}T} \times \frac{\mathrm{d}T}{\mathrm{d}x}.$$
 (1)

Examining the data reproduced in Fig. 2A-E, we find that the maximum velocities observed during the return jump increase with heater wire voltage (1.6 mm s^{-1} , 0.9 mm s^{-1} , and 0.5 mm s^{-1} at 1.00 V, 0.50 V, and 0.10 V, respectively). The observed velocities are within an order of magnitude of those predicted Communication ChemComm

by a continuum model of thermocapillary motion of a bubble in a Hele-Shaw cell derived by Siekmann.²⁹ As the temperature gradient scales with heater power, these results support the thermocapillary hypothesis. In addition, differences in energy of the liquid/solid interfaces (Pt, SiNx, SiO2) drive bubble motion such that more hydrophilic surfaces are preferentially wetted. Because the center of the heater wire is on top of a highly conductive Pt film, Joule heating is greatest in the segments of the wire that sit on the bare window, and the bubbles are driven to these positions of highest temperature by the temperature gradient perpendicular to the heater wire (see Fig. 2A-E and Fig. S4, ESI†). As plasma-cleaned silicon nitride is moderately hydrophilic, it is likely that the positive disjoining pressure formed at a silicon nitride-liquid water-vapor interface results in a truncated water microfilm at the bubble-window interface of several nm thickness.³⁰ This would prevent the formation of a true tripleline, and may serve to enhance bubble mobility. As shown in the last few frames in Fig. 1, the bubble motion is impeded by the edge of the 25 nm platinum trace. This suggests that patterned surface films could be useful in controlling the migration of surface adsorbed bubbles.

Secondary bubble nucleation and subsequent collapse due to Ostwald ripening were repeatedly observed. An example from experiment C is reproduced in Fig. S6 (ESI†). As the second bubble nucleates, the first stops growing momentarily and by displacement of the surrounding liquid rotates it about a pinning point to the heater wire. The pause in growth of the larger bubble is due the local evaporative cooling and consumption of dissolved gas during the secondary nucleation. The difference in Laplace pressures drives the consumption of the second bubble by its larger neighbor. As the unstable smaller bubble collapses, the larger bubble grows in the opposite direction, unlike the behavior of bubbles of \sim 5 nm diameter observed in a graphene TEM cell that move closer and distort significantly during Ostwald ripening.31 It is likely that a gas microjet forms from the implosion of the bubble, but imaging this was beyond the time resolution of our detector. In all observed cases of secondary bubble nucleation, the smaller, secondary bubble is rapidly consumed (Video S1, ESI†). While multi-bubble systems are clearly unstable under the present experimental conditions, the technique should prove useful in examining the stabilization and other collective behaviors associated with heterogeneous gas and water vapor bubbles at the micron scale and below, as long as radiolytic gas generation is properly considered. The secondary bubble in experiment C was the longest lived, with a lifetime of only 35 ms.

In this work, microbubble evolution in water was characterized *in situ* using high-speed liquid cell TEM. During heating with a Pt wire, gas and water vapor are liberated. Bubbles nucleate at surface defects near the region of highest temperature, rapidly migrate away and grow, and are driven back to the heat source by thermocapillary forces. Ostwald ripening, motion, secondary bubble collapse and other phenomena at the millisecond timescale and micron length scale were observed reproducibly. Thermal gradients, dissolved gas, surface geometry (with associated contact-line pinning), and interfacial energies are the key drivers of microbubble evolution.

At practical beam current densities employed in TEM, radiolytic gas production can be a significant driver of bubble growth at elevated temperatures, but evidence of $\rm H_2O$ boiling is also manifest in observed kinetics. Microbubble diameters grow as $\sim t^{0.5}$, with diffusive transport limiting kinetics. These results begin to fill an important experimental knowledge gap relevant to thermally induced bubble evolution, highlighting the complex microscale dynamics of microbubbles on millisecond timescales. The fundamental results are of particular consequence for tailoring site-specific bubble nucleation and directional control in microfluidics and heat exchangers.

We thank James Mabon for his assistance with the TEM and liquid cell. This work was supported by the National Science Foundation under Grant No. 1254406 and was carried out in the Frederick Seitz Materials Research Laboratory Central Research Facilities, University of Illinois.

Notes and references

- 1 L. Bocquet and P. Tabeling, Lab Chip, 2014, 14, 3143.
- 2 D. Lohse and X. Zhang, Rev. Mod. Phys., 2015, 87, 981-1035.
- 3 A. Karbalaei, R. Kumar and H. Cho, Micromachines, 2016, 7, 13.
- 4 L. Lin, Microscale Thermophys. Eng., 1998, 2, 71-85.
- 5 X. Qu and H. Qiu, J. Micromech. Microeng., 2009, 19, 95008.
- 6 L. Lin, X. Peng, Z. Mao, W. Li, M. N. Yogeesh, B. B. Rajeeva, E. P. Perillo, A. K. Dunn, D. Akinwande and Y. Zheng, *Nano Lett.*, 2016, 16, 701–708.
- 7 C. Koji Takahashi and J.-G. Weng, Microscale Thermophys. Eng., 1999, 3, 169–182.
- 8 C. Li, Z. Wang, P. I. Wang, Y. Peles, N. Koratkar and G. P. Peterson, Small, 2008, 4, 1084–1088.
- 9 R. E. Cavicchi and C. T. Avedisian, Phys. Rev. Lett., 2007, 98, 23-26.
- 10 J. N. Chung, T. Chen and S. C. Maroo, Front. Heat Mass Transfer, 2011, 2, 023004.
- 11 S. Jones, Adv. Colloid Interface Sci., 1999, 80, 27-50.
- 12 H. Wang, X.-F. Peng and D. M. Christopher, *Chin. Phys. Lett.*, 2005, 22, 2881–2884.
- 13 E. J. Ching, C. Thomas Avedisian, M. J. Carrier, R. C. Cavicchi, J. R. Young and B. R. Land, Int. J. Heat Mass Transfer, 2014, 79, 82–93.
- 14 T. K. Jun and C.-J. Kim, J. Appl. Phys., 1998, 83, 5658-5664.
- 15 B. Selva, I. Cantat and M.-C. Jullien, Phys. Fluids, 2011, 23, 52002.
- 16 P. Gutfreund, M. Maccarini, A. J. C. Dennison and M. Wolff, Langmuir, 2016, 32, 9091–9096.
- 17 N. F. Bunkin, A. V. Shkirin, I. S. Burkhanov, L. L. Chaikov and A. K. Lomkova, *Quantum Electron.*, 2014, 44, 1022–1028.
- 18 L. Luo and H. S. White, Langmuir, 2013, 29, 11169-11175.
- 19 S.-T. Lou, Z.-Q. Ouyang, Y. Zhang, X.-J. Li, J. Hu, M.-Q. Li and F.-J. Yang, J. Vac. Sci. Technol., B: Microelectron. Nanometer Struct. – Process., Meas., Phenom., 2000, 18, 2573–2575.
- 20 J. M. Grogan, N. M. Schneider, F. M. Ross and H. H. Bau, *Nano Lett.*, 2014, 14, 359–364.
- 21 E. R. White, M. Mecklenburg, S. B. Singer, S. Aloni and B. C. Regan, Appl. Phys. Express, 2011, 4, 055201.
- 22 Y. Liu and S. J. Dillon, Chem. Commun., 2014, 50, 1761.
- 23 C. U. Chan and C.-D. Ohl, Phys. Rev. Lett., 2012, 109, 174501.
- 24 X. H. Zhang, A. Quinn and W. A. Ducker, Langmuir, 2008, 24, 4756-4764.
- 25 N. M. Schneider, M. M. Norton, B. J. Mendel, J. M. Grogan, F. M. Ross and H. H. Bau, J. Phys. Chem. C, 2014, 118, 22373–22382.
- 26 E. A. Stach, D. Zakharov, R. D. Rivas, P. Longo, M. Lent, A. Gubbens and C. Czarnik, *Microsc. Microanal.*, 2013, 19, 392–393.
- 27 A. Botman, M. Hesselberth and J. J. L. Mulders, Microelectron. Eng., 2008, 85, 1139–1142.
- 28 R. Sander, Atmos. Chem. Phys., 2015, 15, 4399-4981.
- 29 J. Siekmann, Acta Mech., 1979, 34, 39-50.
- 30 A. Chatterjee, J. L. Plawsky and P. C. Wayner, *Adv. Colloid Interface Sci.*, 2011, **168**, 40–49.
- 31 D. Shin, J. B. Park, Y.-J. Kim, S. J. Kim, J. H. Kang, B. Lee, S.-P. Cho, B. H. Hong and K. S. Novoselov, *Nat. Commun.*, 2015, 6, 6068.